POLISH MARITIME RESEARCH 3 (127) 2025 Vol. 32; pp. 79-91
10.2478/pomr-2025-0037

HUMAN-MACHINE COOPERATIVE MARINE LIFTING OF SLENDER-BEAM PAYLOAD WITH A MULTI-TAGLINE ANTI-SWAY AND POSITIONING SYSTEM

Maokai Sun[1,2]
Shenghai Wang[1] *
Guangdong Han[1]
Haiquan Chen[1]
Yuqing Sun[1]

[1] Marine Engineering College, Dalian Maritime University, Dalian, China
[2] Department of Naval Architecture, Ocean and Marine Engineering, University of Strathclyde, United Kingdom

* Corresponding author: *shenghai_wang@dlmu.edu.cn (Shenghai Wang)*

ABSTRACT

To address the challenges of low positioning efficiency, difficulty, and high risk in the hoisting and positioning of a slender-beam payload (SBP) under rough sea conditions, a human-machine cooperative lifting method (HMCLM) is proposed for the first time. In this approach, the operator collaborates with a multi-tagline anti-sway and positioning system (MTAPS) to achieve the rapid and precise positioning of the SBP. A dynamic model of the MTAPS is developed based on multibody dynamics and classical Newtonian mechanics; it also considers the operator's safety requirements. Simulation analysis is conducted using MATLAB/Simulink, and the results indicate that the HMCLM achieves approximately a 10% improvement in sway reduction compared to the MTAPS. Furthermore, the experimental results demonstrate that the MTAPS achieves an average sway reduction of 89.7% for the double-pendulum system. The proposed HMCLM enables the rapid and precise offshore positioning of the SBP, offering a novel approach to enhancing the efficiency of offshore hoisting operations.

Keywords: marine crane; slender-beam payload; anti-sway; positioning

INTRODUCTION

With the development of the maritime transportation industry, the demand for offshore lifting operations between ships or between ships and platforms has been steadily increasing. Such operations include offshore cargo handling, container transfer, and the construction and maintenance of offshore platforms [1, 2]. However, due to the interference of environmental loads such as wind, waves, and currents, coupled with the multi-degree-of-freedom motion of ships or floating platforms and the underactuated nature of cranes, payloads exhibit complex dynamic characteristics [3]. These factors pose significant risks to deck personnel and reduce both the efficiency and operational window of lifting tasks. Therefore, developing an effective anti-sway strategy for marine cranes is an urgent requirement to enhance offshore operational capabilities.

Many researchers have conducted extensive studies on anti-sway control for marine cranes, with existing approaches primarily falling into two categories [4]. The first is mechanical control, which involves designing and installing mechanical devices to directly constrain or suppress the payload sway. The second is electronic anti-sway control, which employs linear or nonlinear controllers to suppress payload sway while ensuring a precise transfer to the designated position. Various anti-sway control methods have been proposed to mitigate payload sway in marine crane operations. Yuan et al. designed a mechanical anti-sway device known as Maryland rigging, which utilises a pulley brake mechanism to dissipate payload oscillation energy through friction between the pulley and the cable [5]. Expanding on this concept, Wen et al. developed an optimal control strategy for Maryland rigging to suppress payload sway under ship roll excitation [6]. Further building upon the Maryland rigging system, Kimiaghalam et al. introduced a fuzzy control approach that dynamically adjusts the cable length to mitigate sway induced by ship roll motion, effectively enhancing the overall sway suppression performance [7]. Parker et al. proposed the rider block tagline system (RBTS), which uses two laterally arranged anti-sway cables to exert drag forces on the payload, thereby dissipating the energy of its swing. Compared with electronic anti-sway methods, the RBTS features lower energy consumption [8]. Hu et al. proposed an eight-cable parallel rigging system, which not only supports the payload weight but also effectively suppresses its sway [9]. Additionally, Wang et al. designed a telescopic sleeve anti-sway device that suppresses payload sway through the damping force of internal springs. While it is effective in reducing sway, this device is less suitable for scenarios requiring long cable deployment [10]. Ren et al. proposed a parallel cable-driven payload positioning system and an adaptive anti-swing tension control method to suppress payload sway and improve offshore crane operation stability [11]. Cai et al. proposed a wave-compensated stabilisation platform for marine cranes, enabling precise lifting operations even in harsh sea conditions. However, since this stabilisation platform must support both the crane and the payload simultaneously, it results in high energy consumption, making it unsuitable for heavy-lift operations [12]. Furthermore, Zhu et al. proposed an underactuated cable-driven multi-loop configuration for wave motion compensation and sway suppression, with simulations and experiments validating its effectiveness [13].

Electronic control uses sensors to monitor crane state variables in real time, with control algorithms adjusting actuator parameters to achieve the desired objectives. Park and Le combined proportional-integral-derivative (PID) control with adaptive sliding mode control to design a controller for a container crane with 2 degrees of freedom (DOF) under ship roll motion. The effectiveness of the proposed controller was validated using ADAMS simulation software [14]. Maleki and Singhose proposed an input shaping technique for land-based cranes and applied it to both single-pendulum and double-pendulum crane systems [15]. Martin and Irani designed a series of controllers, including sliding mode and proportional-derivative (PD) controllers, for high-DOF knuckle boom marine cranes, achieving effective sway suppression for the lifted payload [16]. Sun et al. developed a robust controller for a 7-DOF boom crane under ship roll motion. The proposed controller is free from unknown terms and uncertain parameters, significantly improving system robustness, and its asymptotic stability was rigorously proven using Lyapunov stability theory. Neural network control has also been applied to marine crane systems [17].

In the literature on lifting and transferring, Ye and Huang proposed a control method for suppressing the sway and torsion of a slender-beam payload (SBP) during horizontal transportation by a tower crane. This method demonstrated good robustness under various working conditions and system parameter variations [18]. Xia et al. proposed a sliding mode control method to address the full-process handling of an SBP by an overhead crane, and the effectiveness of the method was validated through both simulation and experiments [19]. Garcia et al. developed 2D and 3D eccentric dynamic models for crane lifting operations involving an SBP and experimentally validated the accuracy of these models [20]. Yang et al. established a dynamic model of a flexible SBP lifted by an overhead crane and proposed a control method to suppress the payload's sway and coupled vibrations; this model was also validated through simulation and experimental results [21]. Existing studies show that offshore SBP lifting remains largely unexplored, with human-machine collaborative operations yet to be addressed. This study introduces a novel anti-sway hoisting method that integrates operator intervention with a multi-tagline anti-sway and positioning system (MTAPS), significantly enhancing the positioning accuracy of marine SBP lifting while improving operational efficiency. This method provides a new approach for hoisting and positioning in scenarios that require high-precision SBP operations.

The paper first introduces the structure of the human-machine cooperative lifting method (HMCLM) and its sway suppression principle. Then, a double-pendulum dynamic model for offshore SBP hoisting with the MTAPS is developed. The dynamic characteristics of the dual-pendulum system are analysed through simulations using MATLAB/Simulink. Furthermore, a scaled experimental prototype of offshore SBP hoisting with the MTAPS is constructed. The experimental validation of the dual-pendulum dynamic model confirms the model's accuracy and the effectiveness of the proposed control method.

HUMAN-MACHINE COOPERATIVE LIFTING WITH THE MTAPS

OVERVIEW OF EXISTING RESEARCH

As shown in Fig. 1-1, we previously proposed an MTAS for lifting a regular payload, and the results demonstrated that the MTAS can effectively suppress the swing of such a payload [22]. With the increasing frequency of marine SBP lifting operations, the MTAS was further applied to SBP lifting, as illustrated in Fig. 1-2. Both the simulation and experimental results indicated that the MTAS provides good anti-sway performance for an SBP [23]. However, its effectiveness becomes limited when handling SBPs with greater length and mass. To address this issue, as shown in Fig. 1-3, we proposed the use of an MTAPS for offshore SBP lifting operations. The anti-sway and positioning device (ASPD) integrated within the anti-sway system is a specially designed spreader tailored for SBPs. It features quick-detachment capabilities, enabling the anti-sway system to handle both SBP and regular payload lifting tasks with flexibility. Compared with the MTAS, the MTAPS achieves better sway suppression for longer and heavier SBPs and can quickly eliminate the initial swing angle during the single-point lifting stage [24].

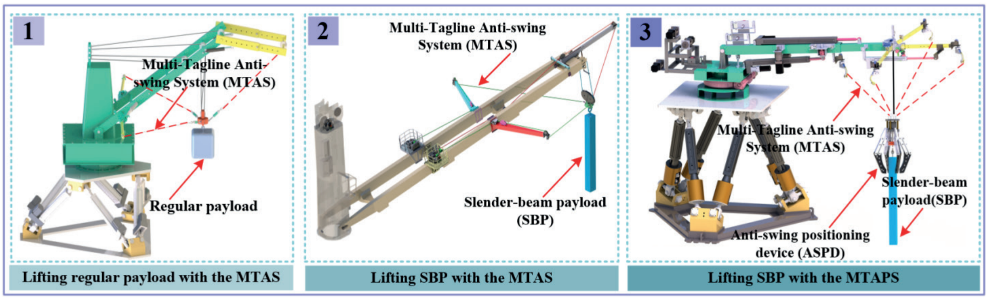

Fig. 1. Overview diagram of existing research

HUMAN-MACHINE COOPERATIVE HOISTING

In operational scenarios where an SBP need to be precisely and vertically positioned onto a ship's hoisting site, relying solely on the MTAPS for positioning may lead to collisions between the SBP and the hoisting site, and accurate alignment cannot be achieved within a short time. Unlike previous studies, this paper proposes, as illustrated in Fig. 2, an HMCLM for the first time, where operators manually guide the SBP using taglines in coordination with the MTAPS to further reduce the sway range of the payload. Specifically, one operator is responsible for controlling the in-plane sway, while the other manages the out-of-plane sway. By applying controlled tension to the taglines, the operators enable the fine-tuned suppression of the payload's motion. The HMCLM combines the mechanical anti-sway capability of the MTAPS with the adaptive responsiveness of human operators, significantly improving the positioning accuracy and operational efficiency of SBP handling.

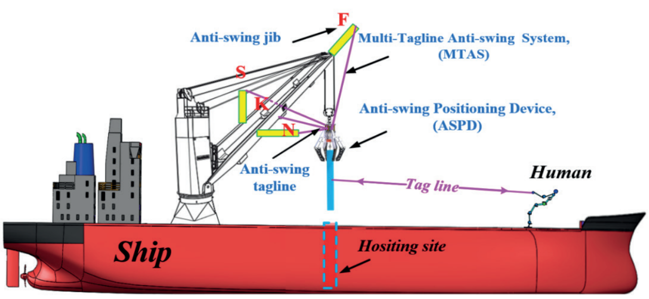

Fig. 2. Illustration of offshore human-machine cooperative lifting with theźMTAPS

DYNAMIC MODELLING OF HUMAN-MACHINE COOPERATIVE LIFTING WITH THE MTAPS

The dynamic modelling of human-machine collaborative SBP lifting with the MTAPS is a prerequisite for studying the dynamics of payload characteristics and designing control strategies. Without loss of generality, the following assumptions are made during the modelling process:

Assumption 1. The hoisting cables, anti-sway taglines, and the taglines used for manual sway suppression are all considered inextensible flexible bodies.

Assumption 2. The MTAPS and the crane's booms are considered rigid structures, and the multi-link clamping mechanism of the ASPD is also modelled as a rigid structure.

Assumption 3. The anchor points and outlet points of the cables are modelled as universal joints, allowing free rotation in all directions.

KINEMATIC MODELLING OF THE MTAPS

To address the modelling of the integrated ship–crane–MTAPS system, Newton-Euler and robotics-based approaches were employed in developing the dynamic model. Fig. 3 illustrates the schematic of human-machine collaborative offshore SBP hoisting with the MTAPS. The reference frames are defined as follows: o_0-$x_0y_0z_0$ represents the earth-fixed frame, o_1-$x_1y_1z_1$ denotes the ship-fixed frame, and o_2-$x_2y_2z_2$ corresponds to the crane-fixed frame. EF represents the retrofitted front anti-sway arm, while HRS and HMN denote the retrofitted left and right anti-sway arms. β_1 refers to the angle between the front anti-sway arm and the crane boom, whereas β_2 represents the angle between the left and right anti-sway arms. P_1F, P_1N, P_1S, and P_1K are the four anti-sway taglines. $\theta_2 y$ represents the luffing angle of the crane, while $\theta_2 z$ denotes its slewing angle. $\theta_1 x$ and $\theta_1 y$ correspond to the ship's roll and pitch motions, respectively. The in-plane sway angle of the ASPD is represented by θ_1, and the out-of-plane angle is represented by ψ_1. Similarly, the in-plane angle of the SBP is denoted as θ_2, and the out-of-plane angle is denoted as ψ_2. The masses of the ASPD and the SBP are denoted as m_1 and m_2, respectively. The length of the crane hoisting cable is represented by L_1, while the distance from the SBP's centre of mass to the lifting point is denoted as L_2.

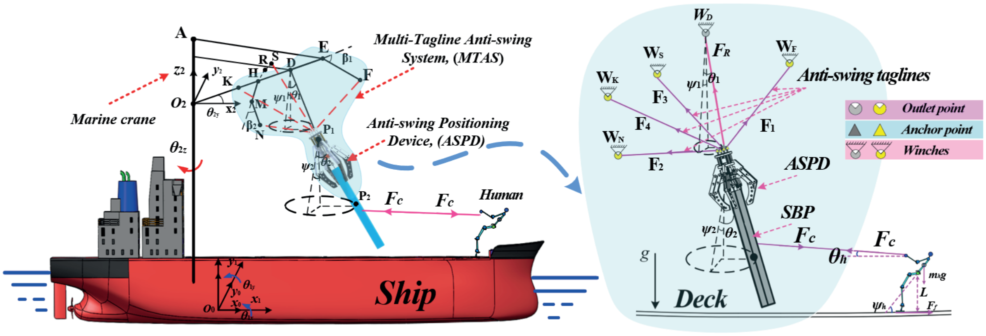

Fig. 3. Simplified diagram of marine human-machine system lifting with the MTAPS

Given the rotation matrices R_x, R_y, and R_z, which represent rotations about the x-axis, y-axis, and z-axis, respectively, the transformation from the (o_n-$x_n y_n z_n$) coordinate frame to the (o_m-$x_m y_m z_m$) coordinate frame can be described using these matrices. Consequently, the coordinates of P_1 in the inertial reference frame can be expressed as

$$ {}_0^1\mathbf{R} = \mathbf{R}_x(\theta_{1x})\mathbf{R}_y(\theta_{1y}) \tag{9}$$

$$ {}_0^2\mathbf{R} = \mathbf{R}_x(\theta_{1x})\mathbf{R}_y(\theta_{1y})\mathbf{R}_z(\theta_{2z}) \tag{10}$$

$$ {}^0\mathbf{P}_{\mathrm{P1}} = {}^0\mathbf{P}_1 + {}_0^1\mathbf{R}^{\mathrm{T}1}\mathbf{P}_2 + {}_0^2\mathbf{R}^{\mathrm{T}2}\mathbf{P}_{\mathrm{P}} \tag{11}$$

${}^0P_1 = [0\ 0\ 0]^T$ represents the coordinates of O_1 in the $x_0y_0z_0$ reference frame, while ${}^1P_2 = [L_x\ L_y\ L_z]^T$ denotes the coordinates of O_2 in the $x_1y_1z_1$ reference frame. By substituting Eq. (1), along with the rotation matrices, into Eq. (11), the expression for P_1 in the $x_0y_0z_0$ reference frame can be obtained.

Let $F_R = [0\ 0\ F_{Rz}]^T$ and $G_P = [0\ 0\ mg]^T$. Define $F_i = [F_{ix}\ F_{iy}\ F_{iz}]^T$ (i = 1, 2, 3, 4), where F_i represents the tension in the i-th anti-sway tagline. The components of the tension F_i along the x_0, y_0, and z_0 axes can be written as

$$\begin{cases} F_{ix} = |F_i| \cdot i_{ix} \\ F_{iy} = |F_i| \cdot i_{iy}, (i = 1,2,3,4) \\ F_{iz} = |F_i| \cdot i_{iz} \end{cases} \tag{12}$$

where $i_{1x} = (x_F - x_{P1})/L_{P1F}$, $i_{1y} = (y_F - y_{P1})/L_{P1F}$, and $i_{1z} = (z_F - z_{P1})/L_{P1F}$. Likewise, the force components of F_2, F_3, and F_4 are obtained using a similar approach. The spatial coordinates of the anti-sway tagline's outlet point can be derived from Eqs. (4) to (7).

The coordinates of the centre of mass of the ASPD and the SBP in the crane-fixed reference frame o_2-$x_2y_2z_2$ are given by

$$ {}^2P_{P_1} = {}^2P_{P_D} + [L_1 \sin\theta_1 \quad -L_1\sin\psi_1 \quad -L_1\cos\theta_1]^{\mathrm{T}} \tag{1}$$

$$ {}^2P_{P_2} = {}^2P_{P_D} + \begin{bmatrix} L_1\cos\psi_1\sin\theta_1 + L_2\cos\psi_2\sin\theta_2 \\ -L_1\sin\psi_1 - L_2\sin\psi_2 \\ -L_1\cos\psi_1\cos\theta_1 - L_2\cos\psi_2\cos\theta_2 \end{bmatrix} \tag{2}$$

D represents the outlet point of the crane hoisting cable on the boom. The coordinates of D in the crane-fixed reference frame can be expressed as

$$ P_D = [L_{O_2D}\cos\theta_{2y} \quad 0 \quad L_{O_2D}\sin\theta_{2y}]^{\mathrm{T}} \tag{3}$$

The outlet points N and S, as well as K and F, are symmetrically positioned in space. The spatial positions of F and K in the crane-fixed reference frame can be expressed as

$$ P_K = [L_{O_2K}\cos\theta_{2y} \quad 0 \quad L_{O_2K}\sin\theta_{2y}]^{\mathrm{T}} \tag{4}$$

$$ \mathrm{P}_F = [L_{O_2E}\cos\theta_{2y} + L_{EF}\cos\beta_1 \quad 0 \quad L_{O_2E}\sin\theta_{2y} - L_{\mathrm{EF}}\sin\beta_1]^{\mathrm{T}} \tag{5}$$

$$ \mathrm{P}_N = [L_{O_2H}\cos\theta_{2y} + L_{MN}\sin\beta_2\cos\theta_{2y} \quad -L_{HM} - L_{MN}\cos\beta_2 \quad L_{O_2H}\sin\theta_{2y} - L_{MN}\sin\beta_2\sin\theta_{2y}]^{\mathrm{T}} \tag{6}$$

$$ \mathrm{P}_S = [L_{O_2H}\cos\theta_{2y} + L_{MN}\sin\beta_2\cos\theta_{2y} \quad L_{HM} + L_{MN}\cos\beta_2 \quad L_{O_2H}\sin\theta_{2y} + L_{MN}\sin\beta_2\sin\theta_{2y}]^{\mathrm{T}} \tag{7}$$

When all anti-sway taglines remain in a taut state, the lengths of the four anti-sway taglines, $L_{P1}F$, $L_{P1}N$, $L_{P1}S$, and $L_{P1}K$, can be expressed as

$$\begin{cases} L_{P_1F} = \sqrt{(x_F - x_{P_1})^2 + (y_F - y_{P_1})^2 + (z_F - z_{P_1})^2} \\ L_{P_1N} = \sqrt{(x_N - x_{P_1})^2 + (y_N - y_{P_1})^2 + (z_N - z_{P_1})^2} \\ L_{P_1S} = \sqrt{(x_S - x_{P_1})^2 + (y_S - y_{P_1})^2 + (z_S - z_{P_1})^2} \\ L_{P_1K} = \sqrt{(x_K - x_{P_1})^2 + (y_K - y_{P_1})^2 + (z_K - z_{P_1})^2} \end{cases} \tag{8}$$

DYNAMIC MODELLING OF THE MTAPS

The crane hoisting cable tension is denoted as F_R, while the tensions in the four anti-sway taglines (I, II, III, and IV) are represented by F_1, F_2, F_3, and F_4, respectively. The masses of the ASPD and the SBP are denoted as m_1 and m_2, respectively. The mass of the ASPD is primarily concentrated at the motor, with its centre of mass represented by P_1, while the centre of mass of the SBP is denoted as P_2.

When the SBP undergoes sway, the components of the crane hoisting cable tension in the x_0, y_0, and z_0 directions can be expressed as

$$\begin{cases} F_{Rx} = |F_R|\cos\psi_1\sin\theta_1 \\ F_{Ry} = |F_R|\sin\psi_1 \\ F_{Rz} = |F_R|\cos\psi_1\cos\theta_1 \end{cases} \tag{13}$$

By conducting a force analysis on the ASPD, its equations of motion can be formulated as

$$\begin{cases} m_1\ddot{x}_{\mathrm{p}_1} = F_{1x} - F_{2x} - F_{3x} + F_{4x} - F_{Rx} + F_{\mathrm{E}x} \\ m_1\ddot{y}_{\mathrm{p}_1} = F_{1y} - F_{2y} - F_{3y} + F_{4y} + F_{Ry} - F_{Ey} \\ m_1\ddot{z}_{\mathrm{p}_1} = F_{1z} - F_{2z} - F_{3z} + F_{4z} + F_{Rz} - \mathrm{m}_1\mathrm{g}\text{-}F_{\mathrm{E}z} \end{cases} \tag{14}$$

Here, F_{Ex}, F_{Ey}, and F_{Ez} represent the forces acting on the SBP.

To simplify the equations, the resultant forces of the four anti-sway taglines in the MTAS along the x-, y-, and z-directions are defined as $f_x = F_{1x}-F_{2x}-F_{3x}+F_{4x}$, $f_y = F_{1y}-F_{2y}-F_{3y}+F_{4y}$, and $f_z = F_{1z}-F_{2z}-F_{3z}+F_{4z}$. By substituting f_x, f_y, f_z and the second derivative of the spatial coordinates at P_1 into Eq. (14), the following expression can be obtained:

$$\begin{cases} m_1\ddot{x}_{P_1} = f_x - |F_R|\cos\,\psi_1 \sin\,\theta_1 + F_{Ex} \\ m_1\ddot{y}_{P_1} = f_y + |F_R|\sin\,\psi_1 - F_{Ey} \\ m_1\ddot{z}_{P_1} = f_z + |F_R|\cos\,\psi_1\cos\,\theta_1 - m_1 g - F_{Ez} \end{cases} \tag{15}$$

F_{Ex}, F_{Ey}, and F_{Ez} represent the forces acting on the SBP in the x-, y-, and z-directions, respectively, and can be expressed as

$$\begin{cases} F_{Ex} = \left[m_2 g\cos\,\theta_2\cos\,\psi_2 + \frac{1}{2}m_2\left(\frac{\dot{\psi}_2\sin\,\psi_2\cos\,\theta_2 + \dot{\theta}_2\sin\,\theta_2\cos\,\psi_2}{\sqrt{1-\cos\,\psi_2\cos\,\theta_2}}\right)^2 L_2\right]\cos\,\psi_2\sin\,\theta_2 \\ F_{Ey} = \left[m_2 g\cos\,\theta_2\cos\,\psi_2 + \frac{1}{2}m_2\left(\frac{\dot{\psi}_2\sin\,\psi_2\cos\,\theta_2 + \dot{\theta}_2\sin\,\theta_2\cos\,\psi_2}{\sqrt{1-\cos\,\psi_2\cos\,\theta_2}}\right)^2 L_2\right]\sin\,\psi_2 \\ F_{Ey} = \left[m_2 g\cos\,\theta_2\cos\,\psi_2 + \frac{1}{2}m_2\left(\frac{\dot{\psi}_2\sin\,\psi_2\cos\,\theta_2 + \dot{\theta}_2\sin\,\theta_2\cos\,\psi_2}{\sqrt{1-\cos\,\psi_2\cos\,\theta_2}}\right)^2 L_2\right]\cos\,\psi_2\sin\,\theta_2 \end{cases} \tag{16}$$

By substituting Eq. (16) into Eq. (15) and further simplifying, we can obtain

$$\begin{cases} \left(f_x + F_{Ex} - m_1\ddot{x}_{\mathrm{P}_1}\right)\tan\,\psi_1 = \left(m_1\ddot{y}_{\mathrm{P}_1} - f_y + F_{\mathrm{Ey}}\right)\sin\,\theta_1 \\ \left(m_1\ddot{y}_{\mathrm{P}_1} - f_y + F_{Ey}\right)\cos\,\theta_1 = \left(m_1\ddot{z}_{\mathrm{P}_1} - f_z + m_1 g\right)\tan\,\psi_1 \end{cases} \tag{17}$$

By solving Eq. (17), the dynamic equations of the ASPD can be derived:

$$\ddot{\theta}_1 = -\sec\,\psi_1\Big(\left(F_{Ex}+f_x\right)\cos\,\theta_1 + \left(-F_{Ex}+f_z\right)\sin\,\theta_1 - \\ - m_1\left(\cos\,\theta_1\ddot{x}_D + \left(g+\ddot{z}_D\right)\sin\,\theta_1 - 2L_1\dot{\theta}_1\dot{\psi}_1\sin\,\psi_1\right)\Big)/m_1 L_1 \tag{18}$$

$$\ddot{\psi}_1 = -\cos\,\theta_1\left(F_{Ez} - f_z + m_1 g + m_1\ddot{z}_D\right)\sin\,\psi_1 - \sin\,\theta_1\sin\,\psi_1\left(F_{Ex} + f_x - m_1\ddot{x}_D\right) + \\ + \cos\,\psi_1\left(F_{Ez} - f_y + m_1\ddot{y}_D - L_1 m_1\dot{\theta}_1^2\sin\,\psi_1\right)/m_1 L_1 \tag{19}$$

Considering the influence of both the ASPD and the manually applied tagline forces on the SBP, the spatial moment equation at the SBP can be expressed as

$$\frac{1}{3}m_2 L_2^2\ddot{\psi}_2 = -\left(\mathrm{m}_2\ddot{y}_{P_2} - F_{gy} - F_{oh}L_{oh}\right)\cos\,\theta_2\cos\,\psi_2 L_2 + \\ + \left(\mathrm{m}_2\ddot{z}_{P_2} + m_2 g\right)\sin\,\psi_2 L_2 \tag{20}$$

$$\frac{1}{3}m_2 L_2^2\ddot{\theta}_2 = \left(\mathrm{m}_2\ddot{x}_{P_2} - F_{gx} - F_{ih}L_{ih}\right)\cos\,\psi_2\cos\,\theta_2 L_2 + \\ + \left(\mathrm{m}_2\ddot{z}_{P_2} + m_2 g\right)\cos\,\psi_2\sin\,\theta_2 L_2 \tag{21}$$

In Eqs. (20) and (21), F_{gx} and F_{gy} represent the reaction forces exerted by the ASPD on the SBP. f_{ih} and f_{oh} denote the manual pulling forces applied by the operators in the in-plane and out-of-plane directions of the SBP, respectively. L_{ih} and L_{oh} represent the distances from the attachment point of the pulling tagline to the hoisting point of the SBP.

By taking the second derivative of the spatial coordinates in Eq. (2), the acceleration at the centre of mass of the SBP can be obtained. By substituting this acceleration into Eqs. (20) and (21), and further solving the equations, the acceleration of the SBP's centre of mass in both the in-plane and out-of-plane directions can be derived:

$$\ddot{\theta}_2 = \left\{-3\cos\,\psi_2\left[\begin{bmatrix} \ddot{x}_D + L_1\cos\,\theta_1\left(\cos\,\psi_1\ddot{\theta}_1 - 2\dot{\theta}_1\dot{\psi}_1\sin\,\psi_1\right) - L_1\sin\,\theta_1 \\ \left[\cos\,\psi_1\left(\dot{\theta}_1^2 + \dot{\psi}_1^2\right) + \ddot{\psi}_1\sin\,\psi_1\right] + L_2\cos\,\theta_2\left(\cos\,\psi_2\ddot{\theta}_2 - 2\dot{\theta}_2\dot{\psi}_2\right. \\ \left.\sin\,\psi_2\right) - L_2\sin\,\theta_2\left[\cos\,\psi_2\left(\dot{\theta}_2^2 + \dot{\psi}_2^2\right) + \ddot{\psi}_2\sin\,\psi_2\right] - f_{gx} - f_{ih}L_{ih} \end{bmatrix}\cos\,\theta_2 + \begin{bmatrix} \ddot{z}_D + L_2\cos\,\psi_2\left[\cos\,\theta_2\left(\dot{\theta}_2^2 + \dot{\psi}_2^2\right) + \ddot{\theta}_2\sin\,\theta_2\right] + L_1(\cos\,\theta_1 \\ \cos\,\psi_1\dot{\theta}_1^2 + \cos\,\theta_1\cos\,\psi_1\dot{\psi}_1^2 + \cos\,\psi_1\sin\,\theta_1\ddot{\theta}_1 + \cos\,\theta_1\sin\,\psi_1 \\ \ddot{\psi}_1 - 2\dot{\theta}_1\dot{\psi}_1\sin\,\theta_1\sin\,\psi_1) + L_2\left(\cos\,\theta_2\ddot{\psi}_2 - 2\dot{\theta}_2\dot{\psi}_2\sin\,\theta_2\right)\sin\,\psi_2 \end{bmatrix}\sin\,\theta_2 + g\sin\,\theta_2\right]\right\}/L_2 \tag{22}$$

$$\ddot{\psi}_2 = \left\{-3\left[\begin{matrix} \left(\ddot{x}_D - L_1\cos\,\psi_1\ddot{\psi}_1 - L_2\cos\,\psi_2\ddot{\psi}_2 + L_1\dot{\psi}_1^2\sin\,\psi_1 + L_2\dot{\psi}_2^2\sin\,\psi_2 - f_{gy} - f_{oh}L_{oh}\right)\cos\,\theta_2 \\ \cos\,\psi_2 - \begin{bmatrix} \ddot{z}_D + L_2\cos\,\psi_2\left(\cos\,\theta_2\left(\dot{\theta}_2^2 + \dot{\psi}_2^2\right) + \ddot{\theta}_2\sin\,\theta_2\right) + L_1(\cos\,\theta_1 \\ \cos\,\psi_1\dot{\theta}_1^2 + \cos\,\theta_1\cos\,\psi_1\dot{\psi}_1^2 + \cos\,\psi_1\sin\,\theta_1\ddot{\theta}_1 + \cos\,\theta_1\sin\,\psi_1 \\ \ddot{\psi}_1 - 2\dot{\theta}_1\dot{\psi}_1\sin\,\theta_1\sin\,\psi_1) + L_2\left(\cos\,\theta_2\ddot{\psi}_2 - 2\dot{\theta}_2\dot{\psi}_2\sin\,\theta_2\right)\sin\,\psi_2 \end{bmatrix}\sin\,\psi_2 + g\sin\,\psi_2 \end{matrix}\right]\right\}/L_2 \tag{23}$$

DESIGN OF THE ANTI-SWAY CONTROLLER

CONTROLLER FOR THE MTAPS

A sway suppression controller for the MTAPS is designed based on the principle of air damping. In this controller, the multiple anti-sway taglines of the MTAPS continuously impede the relative motion of the payload, while the ASPD transmits the forces from the anti-sway taglines to the vicinity of the SBP's centre of mass. The design of the sway suppression controller is as follows:

$$\begin{cases} \text{if} \quad \dot{\theta}_1 > 0 \quad F_{1x} = \delta_{1x} \quad F_{4x} = -K\theta_1 - B\dot{\theta}_1 + F_{1x} \\ \text{if} \quad \dot{\theta}_1 \le 0 \quad F_{4x} = \delta_{4x} \quad F_{1x} = F_{4x} + K\theta_1 + B\dot{\theta}_1 \\ \text{if} \quad \dot{\psi}_1 > 0 \quad F_{3y} = \delta_{3y} \quad F_{2y} = -K\psi_1 - B\dot{\psi}_1 + F_{3y} \\ \text{if} \quad \dot{\psi}_1 \le 0 \quad F_{2y} = \delta_{2y} \quad F_{3y} = F_{2y} + K\psi_1 + B\dot{\psi}_1 \end{cases} \tag{24}$$

In Eq. (24), $K > 0$ and $B > 0$, where K is the stiffness coefficient and B is the damping coefficient. F_{2y} and F_{3y} represent the y-axis force components of anti-sway taglines II and III, corresponding to the control of the in-plane angle (θ) of the SBP. δ_{2y} and δ_{3y} denote the pre-tension components of taglines II and III along the y-axis. Similarly, F_{1x} and F_{4x} represent the x-axis force components of anti-sway taglines I and IV, corresponding to the control of the out-of-plane angle (ψ) of the SBP. δ_{1x} and δ_{4x} denote the pre-tension components of taglines I and IV along the x-axis.

In the MTAPS, the tension of the anti-sway taglines must remain within a reasonable range. If the tension is too low, the taglines may slip out of the winch drum; if the tension is too high, it could overload the anti-sway winches. The tension of the anti-sway taglines is set as

$$F_{is} - \delta_i \leqslant |\boldsymbol{F}_i| \leqslant F_{is} + \delta_i, i = (1,2,3,4) \tag{25}$$

In Eq. (25), F_{is} and δ_i represent the pre-tension and tension threshold of the i-th anti-sway tagline (i = 1, 2, 3, 4), respectively. The pre-tension and tension threshold are determined based on the mass of the SBP for each lifting operation.

HUMAN-MACHINE COOPERATIVE CONTROL

During the positioning phase, operators use tagline manipulation to assist the MTAPS in further reducing the sway amplitude of the SBP. Specifically, one operator is assigned to control the motion in the in-plane direction and another to control the out-of-plane direction. Taking the in-plane motion as an example, when the payload swings away from the operator, they apply a pulling force proportional to the in-plane swing velocity; when the payload swings toward the operator, they merely maintain enough tension to keep the tagline in tension. Similarly, the operator handling out-of-plane motion uses the same tension control strategy:

$$\begin{cases} \text{if} \quad \dot{\theta}_2 > 0 \quad F_{ih} = \delta_{ix} \\ \text{if} \quad \dot{\theta}_2 \leq 0 \quad F_{ih} = -K_i m_2 g \dot{\theta}_2 + \delta_{hx} \\ \text{if} \quad \dot{\psi}_2 > 0 \quad F_{oh} = \delta_{oy} \\ \text{if} \quad \dot{\psi}_2 \leq 0 \quad F_{oh} = -K_o m_2 g \dot{\psi}_2 + \delta_{hy} \end{cases} \tag{26}$$

In this formulation, F_i and F_o represent the forces exerted by humans on the SBP in the in-plane and out-of-plane directions, respectively. Likewise, δ_{ix} and δ_{iy} denote the tensioning forces applied in the in-plane and out-of-plane directions to keep the tagline taut. The parameters K_i and K_o serve as human adjustment coefficients for the in-plane and out-of-plane directions, respectively, and are tied to the maximum pulling force a human can exert.

When operating the tagline, the operator needs sufficient friction against the ground to counteract the horizontal pulling force. If this pulling force becomes too large, foot slippage may occur.

In the simplified model, the support force from the ground on the human body can be approximated as

$$N_h = m_h g - F_{fric} \sin\, \theta_h \tag{27}$$

In this analysis, N_h represents the support force provided by the deck on the human body, m_h denotes the mass of the human body, F_{fric} denotes the maximum pulling force permissible without inducing friction, and θ_h represents the angle between the pulling force and the horizontal direction. When the pulling force acts diagonally upward, it diminishes the normal force between the human and the ground. To prevent slippage, the horizontal force acting on the human must satisfy

$$F_{fric} \cos\, \theta_h \leq \mu\left(m_h g - F_{fric} \sin\, \theta_h\right) \tag{28}$$

μ represents the friction coefficient between the human body and the deck surface.

By rearranging the equations, we can derive the maximum permissible pulling force that ensures the operator remains slip-free:

$$F_{fric} \leq \frac{\mu m_h g}{\cos\, \theta_h + \mu \sin\, \theta_h} \tag{29}$$

Under non-slipping conditions, an excessive pulling force may cause the individual to pitch forward. By employing a simplified rigid-body equilibrium approach and treating the foot as the pivot, we perform a rotational equilibrium analysis of the human body:

$$m_h g L \sin\, \psi_h \leq F_{trip} \cos\, \psi_h H \tag{30}$$

In this formula, ψ_h denotes the angle of the human body's torso relative to the vertical, L is the distance from the pivot to the individual's centre of mass, H is the vertical distance from the pivot to the hands (or the approximate point of application of the pulling force on the body), and F_{trip} represents the maximum allowable pulling force that prevents the human body from tipping over.

The maximum permissible pulling force that prevents the human body from tipping over is

$$F_{trip} \leq \frac{m_h g L \sin\, \psi_h}{H \cos\, \psi_h} \tag{31}$$

To maintain both balance and a slip-free state, the maximum permissible pulling force must fulfil the following condition:

$$F_{\max(\theta_h, \psi_h)} \leq \min\left[\frac{\mu m_h g}{\cos\, \theta_h + \mu \sin\, \theta_h}, \frac{m_h g L \sin\, \psi_h}{H \cos\, \psi_h}\right] \tag{32}$$

As shown in Table 1, the operator's body mass is 80 kg, with a backward inclination angle of 26° and a tension-to--horizontal angle of 10° (indicating an upward pull). The friction coefficient between the feet and the ground is 0.6, and the safety factor is set to 1.2. Under conditions where the operator does not slip or topple, the exerted pulling force is approximately 280 N. This force is used as a reference threshold for human-applied force in subsequent simulations. In practical operations, however, this value should be adjusted to account for individual differences, working conditions, and environmental factors.

Tab. 1. Parameters of the operator

Parameter	Value	Units	Parameter	Value	Units
Human body mass m_h	80	kg	Human backward inclination angle ψ_h	26	°
Human body height	1.76	m	Angle between the tension and the horizontal θ_h	10	°
Ground friction coefficient μ	0.6		Distance from the feet to the body's centre of mass L	0.9	m
Gravitational acceleration g	9.8	m/s^2	Vertical height from the feet to the point of force application H	1.2	m

DYNAMIC SIMULATION ANALYSIS

A simulation analysis was conducted using a COSCO Shipping Group marine crane model, with specific parameters set as follows: $L_{EF} = 4$ m, $L_{HM} = L_{HN} = 2$ m, $L_{OH} = 8$ m, $L_{OD} = 7.6$ m, $L_{OE} = 8.4$ m, and $\beta_1 = \beta_2 = 20°$. The hoisting cable and the SBP measure 2 m and 5 m in length, respectively, with the SBP weighing 600 kg. The simulations were performed under sea states 3 and 4 [25]. The sea state 3 simulation parameters are set as follows: the roll amplitude is 4.6° with a period of 13 s, and the pitch amplitude is 1.2 with a period of 8 s. For sea state 4, the roll amplitude is 6.8° with a period of 13 s, and the pitch amplitude is 1.8° with a period of 7 s. The simulations were executed using MATLAB/Simulink, employing the ode 45 solver.

SIMULATION OF THE POSITIONING PHASE

When a marine crane hoists the SBP to a designated location (hoisting site, as shown in Fig. 2), it is crucial to minimise the sway range of the payload to achieve precise positioning. However, in operational scenarios with even higher positioning accuracy requirements, the use of the MTAPS alone may not be sufficient. In such cases, the HMCLM is required. As illustrated in Figs. 4 and 6, compared with the uncontrolled scenario, the swing angle of the double-pendulum system stabilises at ±1.2° when the MTAPS is used. When the HMCLM is adopted, the swing angle further stabilises at ±0.5°, increasing the average sway reduction efficiency from 81.2% to 92.5%. Consequently, the HMCLM achieves approximately a 10% improvement in sway reduction performance compared to the MTAPS. Additionally, as shown in Figs. 5 and 7, the projection area of the payload during positioning operations is smaller with the HMCLM compared to the MTAPS. This indicates that the HMCLM enables higher-precision positioning tasks.

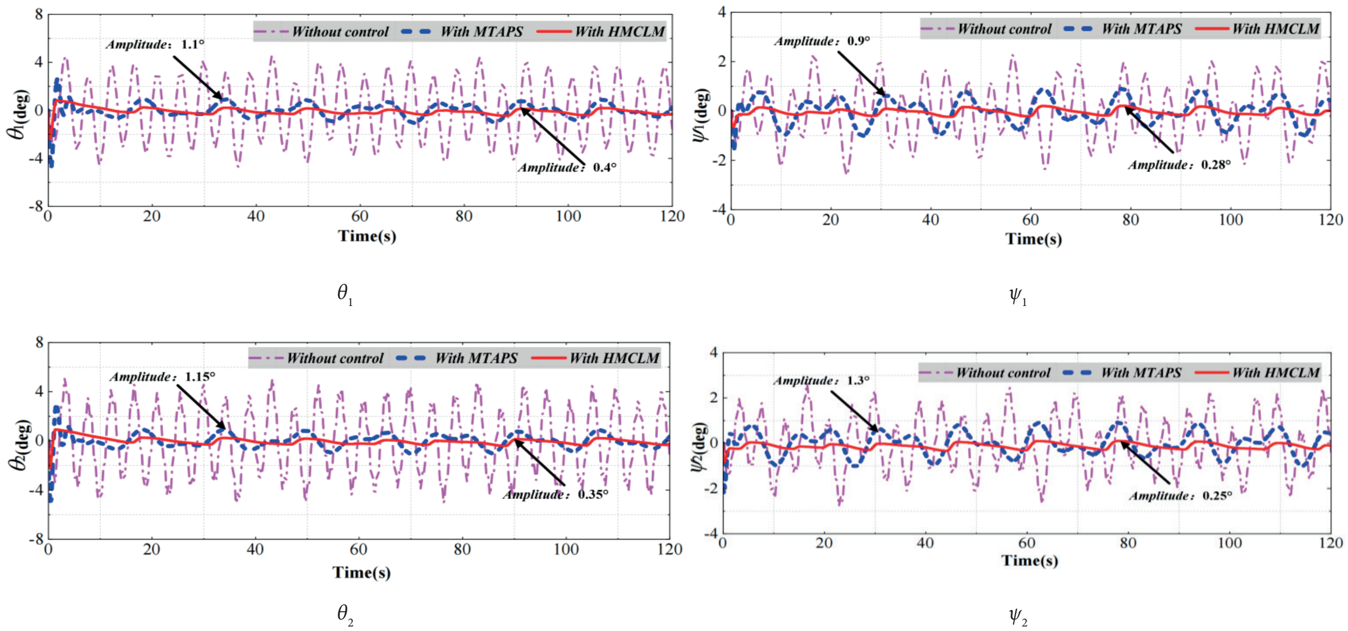

Fig. 4. Comparison curves of dynamic response characteristics during the positioning phase under sea state 3

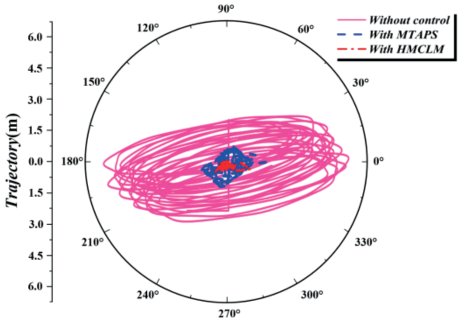

The projected area of the ASPD

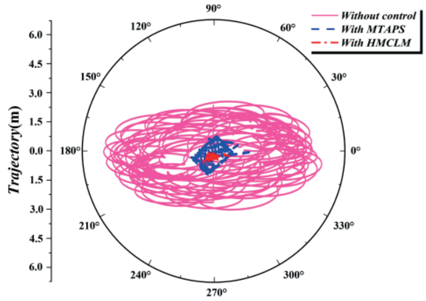

The projected area of SBP

Fig. 5. Comparison of projected areas under sea state 3

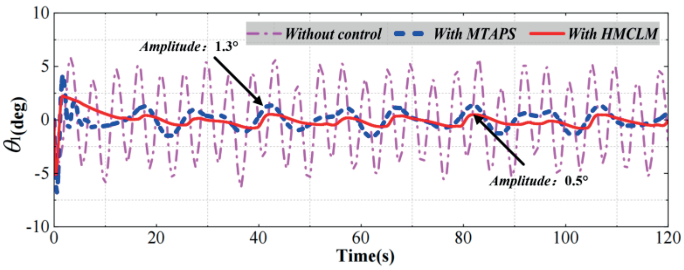

θ_1

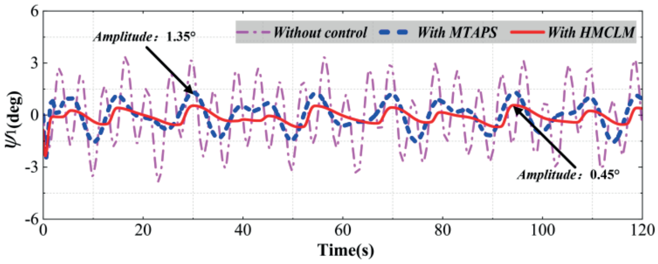

ψ_1

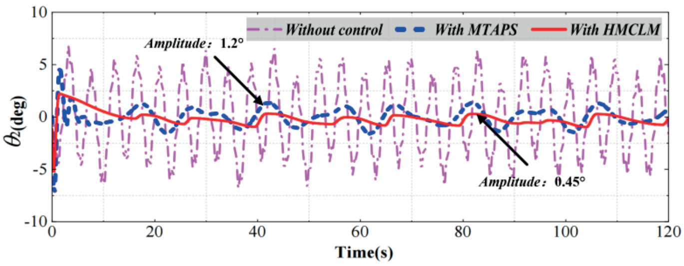

θ_2

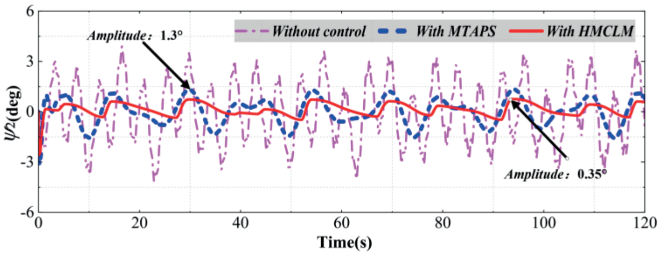

ψ_2

Fig. 6. Comparison curves of dynamic response characteristics during the positioning phase under sea state 4

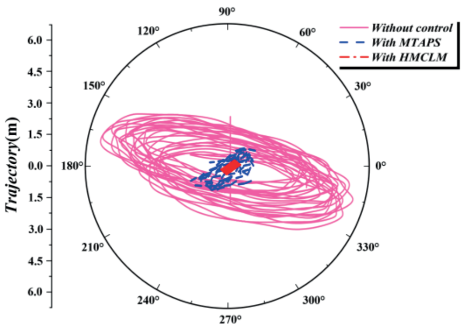

The projected area of the ASPD

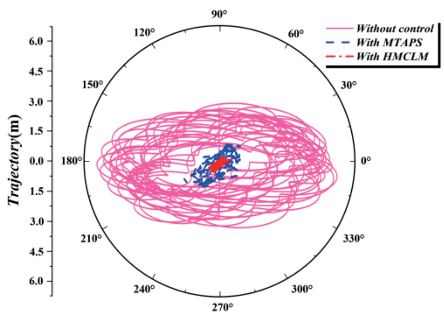

The projected area of SBP

Fig. 7. Comparison of projected areas under sea state 4

SIMULATION OF THE POSITIONING PHASE WITH AN INITIAL SWAY ANGLE

At the initial phase of the hoisting and positioning operation, the SBP experiences an initial sway angle due to the intermittent operation of the crane operator and the payload's inertia. In this simulation, the initial sway angle of the SBP is set to 10°. As shown in Figs. 8 and 9, the HMCLM eliminates the initial sway angle within 5 s while ensuring that the SBP does not undergo frequent oscillations during this process. In contrast, the MTAPS requires approximately 10 s to eliminate the initial sway angle, and during this period, the SBP exhibits frequent oscillations. Comparing the two sway suppression strategies, after the double-pendulum system stabilises following the elimination of the initial sway angle, the residual sway range of the payload under the HMCLM is significantly smaller than that under the MTAPS. This indicates that the HMCLM effectively reduces the likelihood of SBP collisions with deck structures. Moreover, compared to the MTAPS, the HMCLM offers higher hoisting efficiency, making it more suitable for operational scenarios or tasks requiring higher positioning accuracy. Compared with mechanical anti-sway devices such as the RBTS and the Maryland rigging system, the HMCLM maintains the hoisting cable in a vertical orientation throughout the positioning process of the SBP, effectively addressing the issue of excessive rope wear associated with the RBTS and Maryland rigging. Moreover, the HMCLM does not compromise the effective working space of marine cranes during SBP lifting operations.

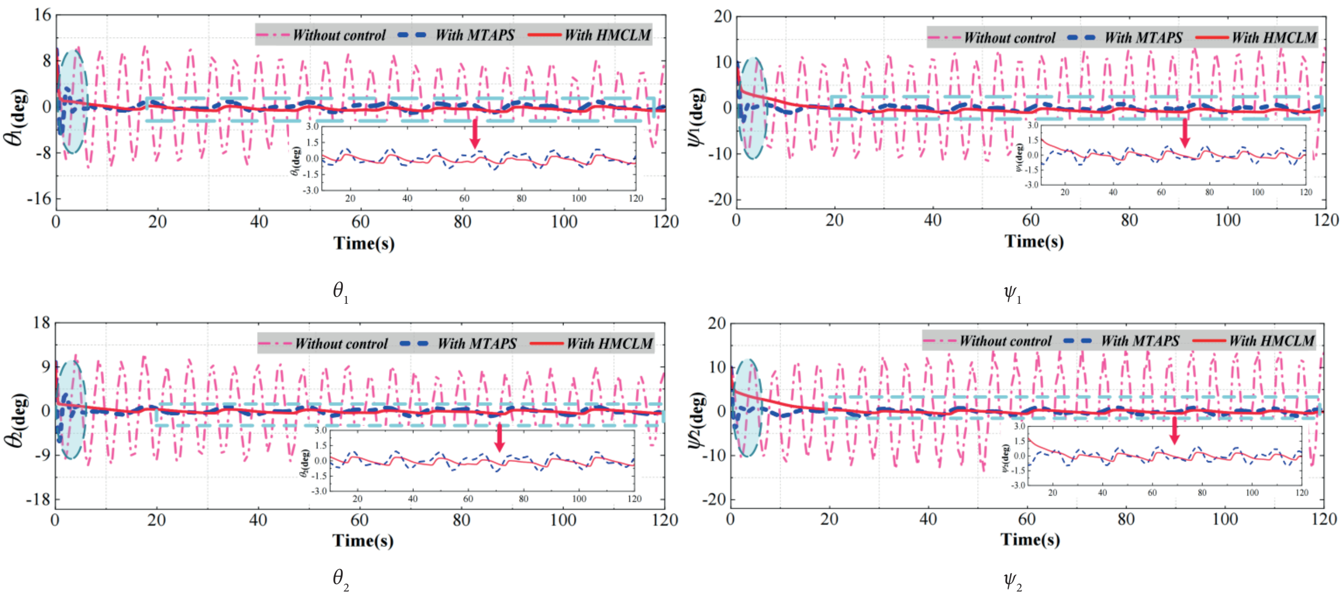

Fig. 8. Comparison of dynamic response characteristics with disturbance under sea state 3

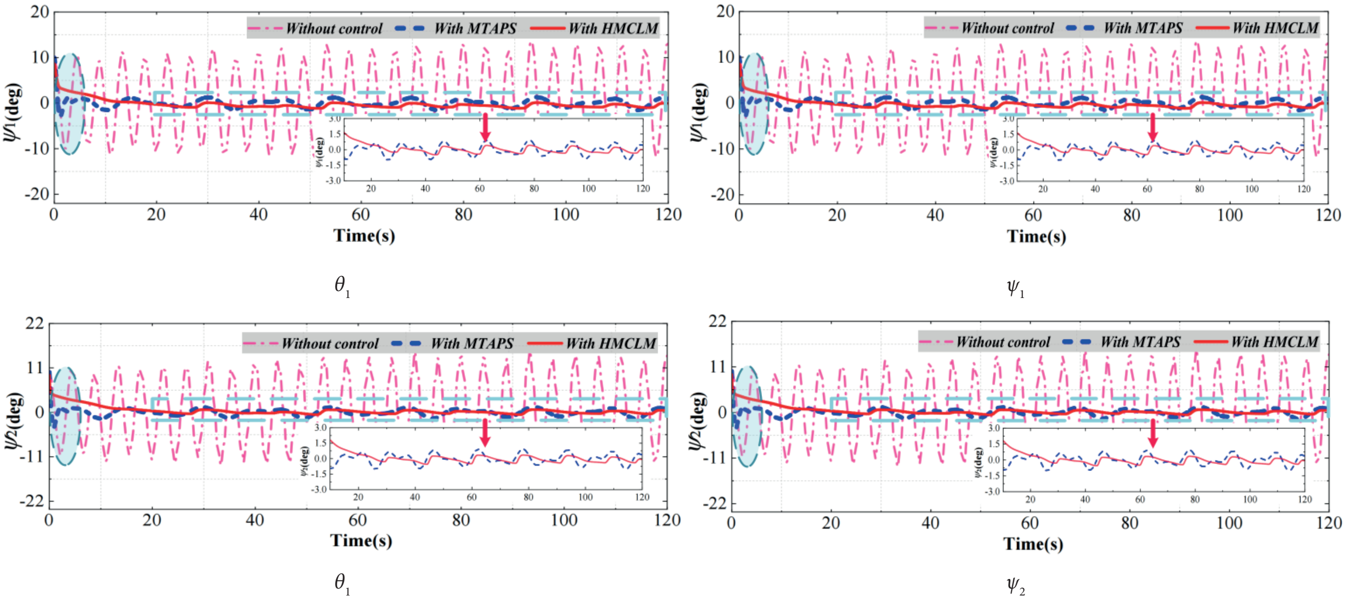

Fig. 9. Comparison of dynamic response characteristics with disturbance under sea state 4

HARDWARE EXPERIMENT

As depicted in Fig. 10, we have constructed a 1:4-scale crane equipped with the MTAPS. The MTAPS comprises the MTAS, which is integrally designed with the crane, and the detachable ASPD. The primary parameters of the scaled prototype are as follows: each of the three anti-sway arms measures 1 m in length; the masses of the ASPD and the SBP are 5 kg and 10 kg, respectively; and the hoisting cable has a length of 1.2 m. To simulate ship motion excitation, the Stewart platform is programmed with angular displacements of $\theta_{1x} = 4\sin(\pi t/3)$ and $\theta_{1y} = 3\sin(\pi t/5)$.

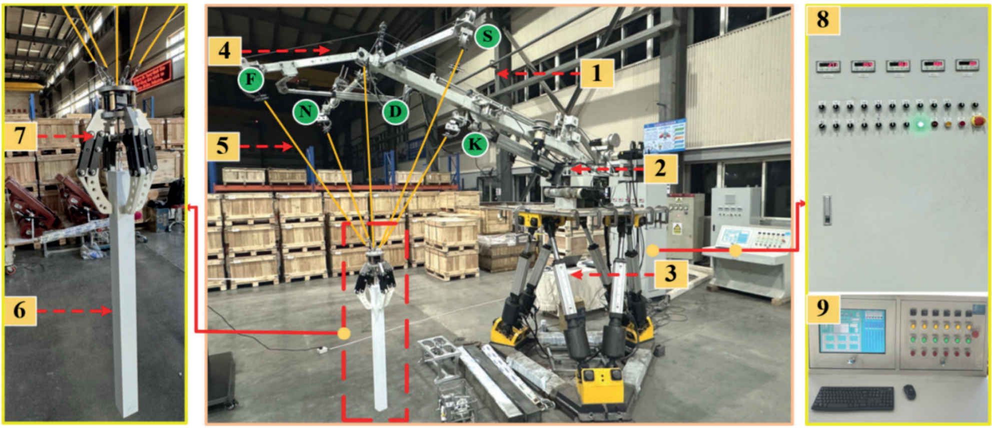

1 – Crane body; 2 – Winches; 3 – Stewart platform; 4 – Anti-swing arm; 5 – Anti-swing taglines; 6 – SBP; 7 – ASPD; 8 – Programmable Logic Controller (PLC) control cabinet; 9 – Stewart platform control system

Fig. 10. The scaled experimental prototype equipped with the MTAPS

DYNAMIC SIMULATION AND EXPERIMENTAL VALIDATION

Simulation and experimental validation were conducted under ship motion excitation, ensuring that the system parameters in the simulations matched those of the scaled crane. Fig. 11 presents a comparison between the experimental and simulation results of the stabilised double-pendulum motion with anti-sway control. The figure demonstrates that, once stabilised, the oscillation angles of both the ASPD and the SBP remain within a 1.2° range. Moreover, the close alignment between the experimental and simulation curves confirms the accuracy of the dynamic model and the effectiveness of the control strategy.

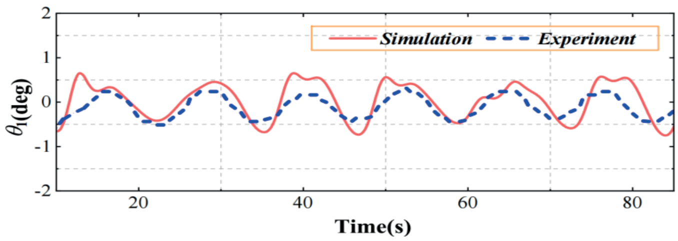

(a) Comparison of experimental and simulation curves for θ_1

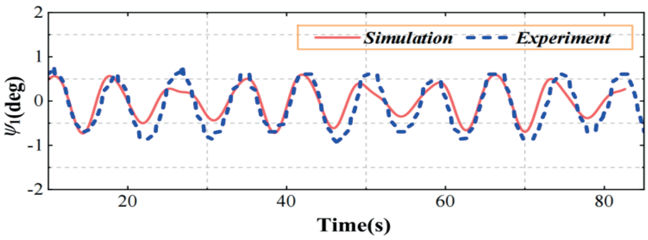

(b) Comparison of experimental and simulation curves for ψ_1

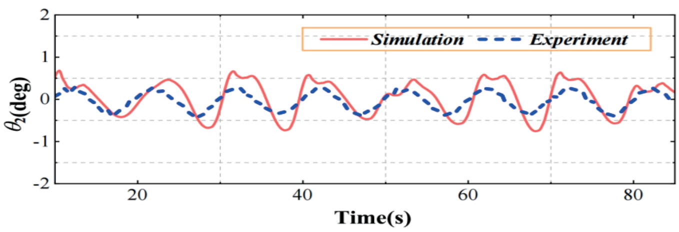

(c) Comparison of experimental and simulation curves

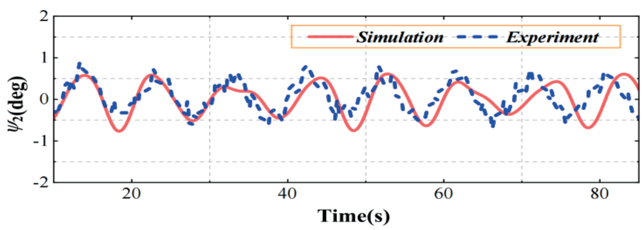

(d) Comparison of experimental and simulation curves for ψ_2.

Fig. 11. Comparison of experimental and simulation curves with the MTAPS

WITH AND WITHOUT ANTI-SWAY EXPERIMENT COMPARISON

Fig. 12 presents a comparative analysis of crane operations with and without the implementation of the MTAPS anti-sway control. The data from Fig. 11 have been reorganised into Table 2. The results indicate that, for the double-pendulum system comprising the ASPD and SBP, the MTAPS achieves an average swing angle reduction of 89.7%. Specifically, the swing angle at the ASPD is reduced by 89.5%, while at the SBP, it is reduced by 90%. This significant reduction enables crane operators to perform rapid transfers and precise positioning of the SBP in offshore environments, thereby enhancing hoisting efficiency.

CONCLUSION

This study addresses the challenges of poor positioning accuracy and low efficiency in the offshore hoisting and positioning of an SBP by introducing the HMCLM for the first time. A dynamic model of marine SBP hoisting with the MTAPS is developed, taking into account the operator's safety conditions. The dynamics of the dual-pendulum system are analysed through simulations, and finally, experiments are conducted to validate the accuracy of the model and the effectiveness of the proposed control method.

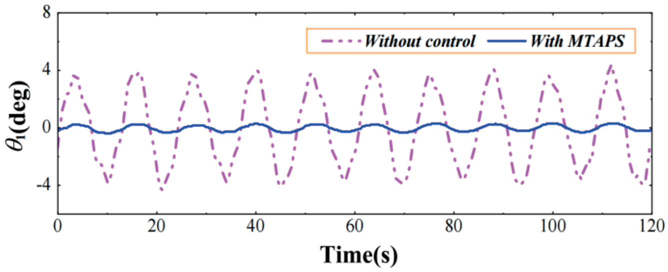

Experimental comparison of θ_1

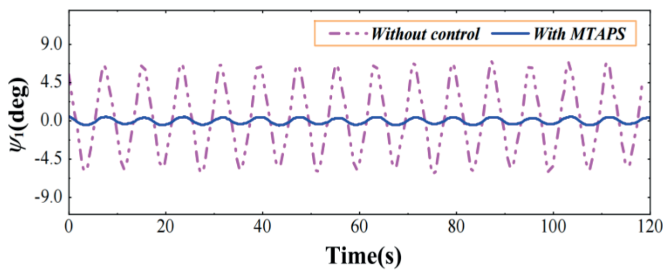

Experimental comparison of ψ_1

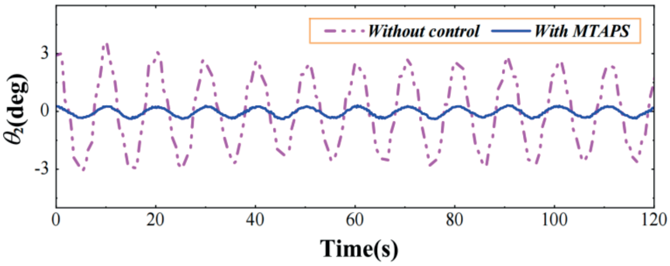

Experimental comparison of θ_2

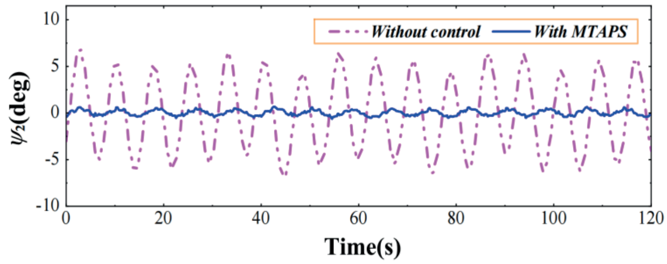

Experimental comparison of ψ_2

Fig. 12. Experimental comparison with and without anti-sway control

Table 2. Anti-sway experiment results for crane with the MTAPS

Scenario	Angle type	Without control (°)	With the MTAPS (°)	Sway angle reduction ratio (%)	Average sway angle reduction ratio (%)
$\theta 1x = 6\sin(\pi t/5)$, $\theta_{1y} = 4\sin(\pi t/6)$	θ_1	3.87	0.45	88	89.7
	ψ_1	6.64	0.61	91	
	θ_2	3.75	0.37	90	
	ψ_2	6.68	0.62	90	

This study accounts for the time-varying motions of the ship and crane, and the dual-pendulum dynamics of the SBP and ASPD, as well as the operator's safety. A precise dynamic model of the human-machine cooperative hoisting system is developed using classical Newtonian mechanics and multibody dynamics.

The dynamic simulation results indicate that compared to using the MTAPS alone, the HMCLM achieves approximately a 10% improvement in sway reduction. Additionally, it rapidly eliminates the initial sway angle induced by external disturbances, effectively preventing the SBP from colliding with deck structures.

Partial experimental verification confirms the accuracy of the MTAPS dynamic model and the effectiveness of the damping control method. Under ship motion excitation provided by the Stewart platform, the MTAPS achieves an average sway suppression effectiveness of over 89.7% for the dual-pendulum system comprising the ASPD and SBP.

The HMCLM proposed in this study enables the rapid and precise positioning of SBPs in offshore environments, offering a new approach to offshore SBP lifting operations. In future work, we plan to develop more effective anti-sway controllers while taking into account rigid-flexible coupling within the system, actual sea conditions, and other influencing factors.

DECLARATIONS

DISCLOSURE STATEMENT

No potential conflicts of interest were reported by the authors.

REFERENCES

1. Li H, Wang B, Li G, Cui Y, Su O, Feng Y, Meng H, Li Y. Response analysis of slender structures on a spar-type floating offshore wind turbine under three types of freak waves. Ocean Engineering 2025. https://doi.org/10.1016/j.oceaneng.2025.120867.

2. Buczkowski R, Zylinski B. Finite element fatigue analysis of unsupported crane. Polish Maritime Research 2021. https://doi.org/10.2478/pomr-2021-0012.

3. Cui Y, Li Y, Li G, Feng Y, Li H, Wang B, Meng H, Deng W. Dynamic response and nonlinear resonance of cylindrical FPSO with a ring groove considering time-varying restoring stiffness. Ocean Engineering 2025. https://doi.org/10.1016/j.oceaneng.2025.120857.

4. Sun M, Zhao T, Wang S, Han G, Jin G, Chen H, Sun Y. Dynamic analysis and experimental research on slender-beam payload swing suppression for marine crane retrofitted a multi-tagline parallel anti-swing system. Ocean Engineering 2024. https://doi.org/10.1016/j.oceaneng.2024.116922.

5. Yuan GH, Hunt BR, Grebogi C, Ott E, Yorke JA, Kostelich EJ. Design and control of shipboard cranes. International Design Engineering Technical Conferences and Computers and Information in Engineering Conference, 1997. https://doi.org/10.1115/DETC97/VIB-4095.

6. Wen B, Homaifar A, Bikdash M, Kimiaghalam B. Modeling and optimal control design of shipboard crane. Proceedings of the 1999 American Control Conference, 1999. https://doi.org/10.1109/ACC.1999.782897.

7. Kimiaghalam B, Homaifar A, Bikdash M. Feedback and feedforward control law for a ship crane with Maryland rigging system. Proceedings of the 2000 American Control Conference. ACC, 2000. https://doi.org/10.1109/ACC.2000.876660.

8. Parker G, Graziano M, Leban F, Green J, Bird JD. Reducing crane payload swing using a rider block tagline control system. OCEANS 2007-Europe, 2007. https://doi.org/10.1109/OCEANSE.2007.4302399.

9. Hu Y, Tao L, Lv W. Anti-pendulation analysis of parallel wave compensation systems. Part M: Journal of Engineering for the Maritime Environment 2016. https://doi.org/10.1177/1475090214558349.

10. Wang J, Wang S, Chen H, Niu A, Jin G. Dynamic modeling and analysis of the telescopic sleeve antiswing device for shipboard cranes. Mathematical Problems in Engineering 2021. https://doi.org/10.1155/2021/6685816.

11. Ren Z, Huang Z, Zhao T, Wang S, Sun Y, Chen H, Fang N. Dynamic modelling and experimental analysis of an offshore crane payload positioning system with a parallel cable-driven method. Polish Maritime Research 2024. https://doi.org/10.2478/pomr-2024-0019.

12. Cai Y, Zheng S, Liu W, Qu Z, Zhu J, Han J. Sliding-mode control of ship-mounted Stewart platforms for wave compensation using velocity feedforward. Ocean Engineering 2021. https://doi.org/10.1016/j.oceaneng.2021.109477.

13. Zhu B, Zhao T, Tang Z, Ding S, Li E. Hierarchical coupling control of cable-driven multi-loop crane for underactuated positioning. International Journal of Mechanical Sciences 2023. https://doi.org/10.1016/j.ijmecsci.2023.108620.

14. Park H-S, Le N-T. Modeling and controlling the mobile harbour crane system with virtual prototyping technology. International Journal of Control, Automation and Systems 2012. https://doi.org/10.1007/s12555-012-0615-y.

15. Maleki E, Singhose W. Swing dynamics and input-shaping control of human-operated double-pendulum boom cranes. Journal of Computational and Nonlinear Dynamics 2012. https://doi.org/10.1115/1.4005933.

16. Martin IA, Irani RA. The examination of operator performance when controlling a shipboard crane anti-sway control system within a virtual-reality simulator. Ocean Engineering 2024. https://doi.org/10.1016/j.oceaneng.2024.117164.

17. Sun N, Fang Y, Chen H, Wu Y, Lu B. Nonlinear antiswing control of offshore cranes with unknown parameters and persistent ship-induced perturbations: Theoretical design and hardware experiments. IEEE Transactions on Industrial Electronics 2017. https://doi.org/10.1109/TIE.2017.2767523.

18. Ye J, Huang J. Analytical analysis and oscillation control of payload twisting dynamics in a tower crane carrying

a slender payload. Mechanical Systems and Signal Processing 2021. https://doi.org/10.1016/j.ymssp.2021.107763.

19. Xia M, Wang X, Wu Q. Modeling and anti-sway control method for vertical lift-up/lay-down process of slender-beam payload. ISA Transactions 2024. https://doi.org/10.1016/j.isatra.2024.04.016.

20. Garcia A, Singhose W, Ferri A. Dynamics and control of off-centered crane lifts. IEEE, 2015.

21. Yang C, Huang J, Singhose W. Dynamic modeling and oscillation control of industrial cranes transporting upright slender flexible payloads. Mechanical Systems and Signal Processing 2024. https://doi.org/10.1016/j.ymssp.2024.111676.

22. Wang S-H, Ren Z-P, Du J-L, Chen H-Q, Sun Y-Q. Payload swing suppression for offshore cranes using a novel triple-tagline system: Theory and experiment. Part M: Journal of Engineering for the Maritime Environment 2020. https://doi.org/10.1177/1475090219874546.

23. Sun M, Wang S, Han G, Jin G, Li J, Chen H, Sun Y. Multi-cable anti-swing system for cranes subject to ship excitation and wind disturbance: Dynamic analysis and application in engineering. Ocean Engineering 2023. https://doi.org/10.1016/j.oceaneng.2023.114518.

24. Sun M, Deng W, Sun Z, Han G, Wang S, Zhang H, Wei Y, Sun Y, Yuan Z. Dynamic analysis and experimental testing of a multi-tagline anti-sway and positioning system for slender-beam payload lifting during offshore operations. Ocean Engineering 2025. https://doi.org/10.1016/j.oceaneng.2024.119790.

25. Love L. Compensation of wave-induced motion and force phenomena for ship-based high performance robotic and human amplifying systems. Office of Scientific & Technical Information Technical Reports, 2003.